ANNUAL REVIEWS

Annual Review of Fluid Mechanics

Rate Effects in Hypersonic Flows

Graham V. Candler

Department of Aerospace Engineering and Mechanics, University of Minnesota, Minneapolis, Minnesota 55455, USA; email: candler@umn.edu

Annu. Rev. Fluid Mech. 2019. 51:379–402

First published as a Review in Advance on September 19, 2018

The *Annual Review of Fluid Mechanics* is online at fluid.annualreviews.org

https://doi.org/10.1146/annurev-fluid-010518-040258

Keywords

hypersonic aerodynamics, aerothermodynamics, high-temperature gas dynamics, nonequilibrium flows, finite-rate processes

Abstract

Hypersonic flows are energetic and result in regions of high temperature, causing internal energy excitation, chemical reactions, ionization, and gas-surface interactions. At typical flight conditions, the rates of these processes are often similar to the rate of fluid motion. Thus, the gas state is out of local thermodynamic equilibrium and must be described by conservation equations for the internal energy and chemical state. Examples illustrate how competition between rates in hypersonic flows can affect aerodynamic performance, convective heating, boundary layer transition, and ablation. The conservation equations are outlined, and the most widely used models for internal energy relaxation, reaction rates, and transport properties are reviewed. Gas-surface boundary conditions are described, including finite-rate catalysis and slip effects. Recent progress in the use of first-principles calculations to understand and quantify critical gas-phase reactions is discussed. An advanced finite-rate carbon ablation model is introduced and is used to illustrate the role of rate processes at hypersonic conditions.

1. INTRODUCTION: THE HYPERSONIC FLOW ENVIRONMENT

A flow is typically considered hypersonic if its Mach number is greater than five. The Mach number is the ratio of the flow speed to the sound speed, and the square of the Mach number is proportional to the ratio of the kinetic energy to the internal energy of the flowing gas. When a hypersonic flow is brought to rest or passes through a shock wave, much of its kinetic energy is converted to internal energy and the temperature increases. Thus, hypersonic flows are energetic and are characterized by high temperatures. For example, when the Space Shuttle orbiter reentered the Earth's atmosphere, it was traveling at 7.5 km/s or about Mach 25, and the kinetic energy of the flow was approximately 124 times greater than the thermal energy of the free-stream gas.

In addition to planetary-entry flows, there is interest in the development of vehicles capable of sustained hypersonic flight in the atmosphere, which is driving the development of hypersonic gliders and air-breathing scramjet-powered systems. Many of the current areas of research in hypersonic aerodynamics and aerothermodynamics are discussed in a recent article (Leyva 2017). Another recent article reviews key fluid dynamics issues associated with the operation of scramjets (Urzay 2018). An older review of planetary entry gas dynamics is also relevant (Gnoffo 1999).

Figure 1 illustrates several hypersonic flows: the 1960s-era X-15 Mach 6.7 rocket plane, a generic lifting hypersonic vehicle, and the Mars Science Laboratory capsule flying at 6 km/s in the Mars atmosphere. The latter two images are from computational fluid dynamics (CFD) simulations of the flow field, and both visualize the temperature on the flow symmetry plane. The hypersonic speeds result in high temperatures in the shock layer that envelops the vehicle and in the boundary layer where there are extreme levels of shear.

The elevated temperatures in hypersonic flows give rise to many processes, such as vibrational and electronic energy excitation, chemical reactions, ionization, and gas-surface interactions. When these processes occur, the perfect gas shock relations are no longer valid and the equations of state become nontrivial. For example, a Mach-6 normal shock wave produces conditions such that the vibrational energy is excited to about 10% of the total internal energy. At higher Mach numbers, additional processes become important, and therefore hypersonic flows are

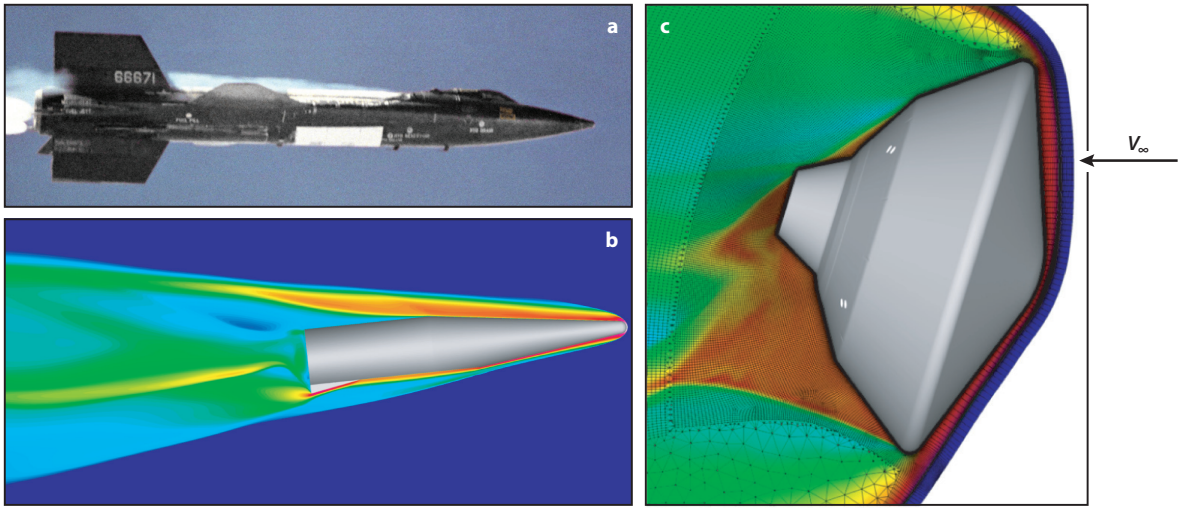

Figure 1

Visualizations of three hypersonic flows: (*a*) the NASA X-15, (*b*) a generic lifting hypersonic body, and (*c*) the Mars Science Laboratory capsule at Mars entry conditions. Panel *a* courtesy of NASA.

usually characterized by imperfect gas effects. The rates of vibrational excitation and chemical reactions depend on the local thermodynamic state, and these rates increase with increasing density and temperature. At typical hypersonic conditions, these rates are often similar to the advection rates.

In this review, we discuss the effects of the internal energy relaxation and chemical reaction rate processes on hypersonic flows. We see that it is seldom possible to assume that the gas is in a state of local thermodynamic equilibrium; rather, the thermodynamic state changes as the gas responds to rapid compressions and expansions. Several examples are provided to illustrate what happens in a typical hypersonic flow and to motivate the development of the governing equations and the scaling properties of these flows. Specific examples of interactions between finite-rate gas-phase and gas-surface reactions are discussed. These include the interaction of acoustic disturbances and vibrational energy relaxation, chemical freezing in high-enthalpy wind tunnel nozzles, and control flap effectiveness at hypersonic flight conditions.

1.1. Gas-Phase Processes

Let us consider a typical hypersonic environment to illustrate the types of gas-phase rate processes that occur in these flows. **Figure 2** shows CFD simulations (see Candler et al. 2014, 2015) of 5-km/s airflow over a 0.1-m radius sphere-cone geometry at three altitudes (40 km, 60 km, and 80 km). The primary difference between each case is the free-stream density, which decreases by a factor of 13.4 between altitudes of 40 and 60 km and by a factor of 18.3 between 60 and 80 km. These differences in density and the corresponding differences in pressure have significant effects on the rate processes and the resulting flow field. The free-stream conditions are given in **Table 1**.

First, consider the 40-km altitude case. Note that there is a strong shock wave that separates the free-stream flow from the high-temperature gas that envelops the sphere-cone geometry. This shock wave is commonly called a bow shock, due to a vague similarity to the bow wave in front of a boat. On the centerline the bow shock is normal, and its strength decreases with increasing distance from the centerline. The shock heats the gas to a temperature of about 6,000 K in this region; this is a significantly lower level than given by perfect-gas normal shock theory, which predicts a temperature of 12,300 K. This difference in temperature is due to internal energy excitation, chemical reactions, and ionization, which absorb energy and reduce the postshock temperature. All of these processes take place at rates that depend on the local flow state. We see that in hypersonic flows, these rates are often similar to the advection rate. Thus, a reaction may be initiated at one point in a flow field, but not reach completion before the gas has moved to a location with a different thermodynamic state.

Now consider the evolution of the flow along the streamline highlighted in the figure. The postshock pressure is about 0.86 bar, and the temperature jumps to about 10,000 K before rapidly dropping to 5,500 K. Two temperatures are plotted: the translational–rotational temperature, T, and the vibrational–electronic temperature, T_{ve}. In the present model, it is assumed that the rotational energy modes of the gas molecules are in equilibrium with the translational or thermal modes. However, the internal energy in the vibrational and electronic modes is allowed to evolve at its own rate, and its energy is characterized by T_{ve}. This is a two-temperature representation of the gas energy state. In the present case, the two temperatures are close to being equilibrated with one another.

After passing through the shock, the gas rapidly expands as it accelerates around the spherical nose, which causes the pressure and temperature to drop before reaching approximately constant values on the conical section of the body. Note that the gas has significant levels of reaction, with O_2 almost fully dissociated and N_2 7.3% dissociated. Nitric oxide (NO) is present at about the

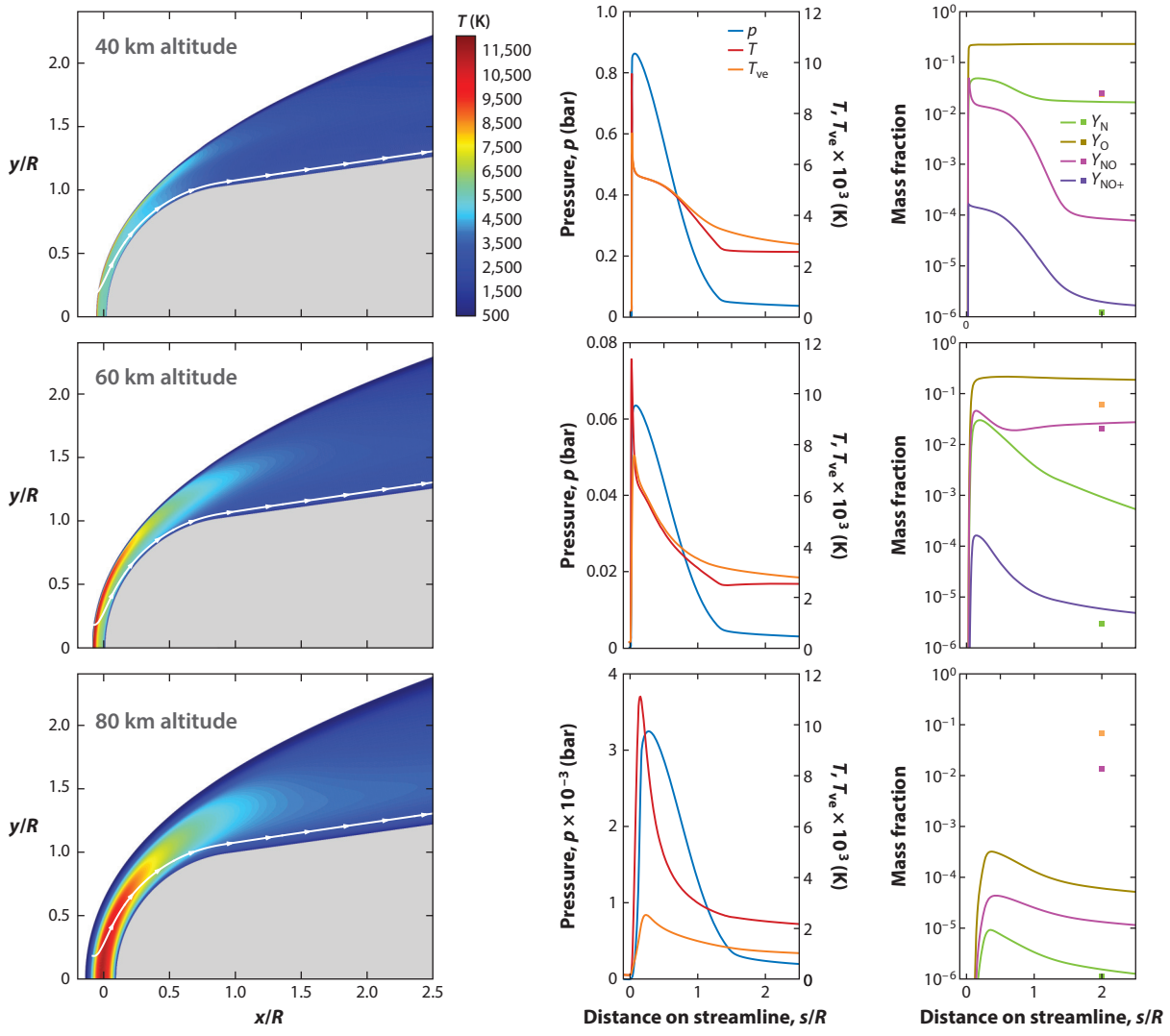

Figure 2

Temperature contours in the flow field of a sphere-cone at three altitudes and a speed of 5 km/s (*left*), along with flow properties extracted on the streamline (*center* and *right*). The symbols at $s/R = 2$ in the mass fraction plots (*right*) denote the equilibrium state of air at the local p, T. Variables: p, pressure; R, nose radius (10 cm); s, distance along the streamline; T, translational–rotational temperature; T_{ve}, vibrational–electronic temperature; Y, mass fraction.

Table 1 Free-stream conditions for example sphere-cone cases

Altitude (km)	Density (kg/m^3)	Temperature (K)	Pressure (Pa)	Mach number	Mean free path (μm)
40	3.85×10^{-3}	251	278	15.7	19.7
60	2.88×10^{-4}	245	20.3	15.9	261
80	1.57×10^{-5}	197	0.886	19.9	4,430

1% level, and its ion, NO^+, at a much lower level. This is the most prevalent ionized species at the present conditions.

In the high-pressure region immediately behind the shock, the gas is in local thermodynamic equilibrium. However, at $s/R = 2$, the gas state is far from equilibrium, with four orders of magnitude more N atoms present than predicted by equilibrium. This out-of-equilibrium, or nonequilibrium, state is a result of the rapid expansion of the gas around the body. The drop in pressure and temperature results in a sudden reduction in the chemical recombination rate, and the gas is approximately frozen near its postshock thermochemical state. Thus, there is a competition between the reaction and advection rates; this is one of the main features of hypersonic flows.

Now let us compare the 40-km altitude flow field with the higher-altitude cases. At 60 km, the flow field is generally similar, but the elevated temperature region behind the shock wave is more pronounced, and the postshock temperature is higher, reaching about 11,400 K. The vibrational–electronic modes are close to equilibrium until the gas expands, then T_{ve} lags the change in T. Also note that at $s/R = 2$, there are three orders of magnitude more N atoms than predicted by local thermodynamic equilibrium. These differences are due to the lower pressure and density at this altitude, which result in reduced rates of internal energy relaxation and chemical reaction.

At 80 km, the flow field is significantly different, with a more diffuse bow shock wave and a large region of elevated temperature. The shock standoff distance is also notably larger. The vibrational–electronic temperature lags the translational–rotational temperature at all locations on the extracted streamline. The level of dissociation is greatly reduced, and at $s/R = 2$, there are fewer N and O atoms than predicted by equilibrium. This is caused by the low-density free-stream conditions, which suppress the reaction rates, resulting in subequilibrium levels of reaction throughout the flow field. Thus, this case is significantly different than the previous two.

1.2. Gas-Surface Processes

We have seen that the gas-phase processes of internal energy excitation, chemical reactions, and ionization affect hypersonic flows. There is another important class of rate process in these flows—the interaction of the high-temperature gas with surfaces. Depending on the surface material properties and the relative reaction rates, the heat transfer rate to the surface can be significantly affected. Several examples are discussed.

Consider the heat transfer rate from the high-temperature air to the sphere-cone geometry discussed above. We have performed two sets of simulations: one with an inert, noncatalytic surface, and a second with a catalytic surface that promotes recombination of those N and O atoms that impinge on the surface. We use an isothermal surface temperature of 1,000 K for both cases. The details of the catalytic gas-surface interaction boundary condition are discussed below.

Figure 3 quantifies the heat transfer rate to the surface as a function of the distance from the stagnation point for the three altitudes considered previously. At 40 km, the catalytic boundary condition increases the stagnation-point heat flux by 64% relative to the noncatalytic surface. This occurs because when the atoms recombine on the surface, the chemical bond energy is deposited on the surface. **Figure 3** also shows how the temperatures and mass fractions vary with distance from the surface along the stagnation streamline (on the symmetry axis). Note that the 40-km noncatalytic case has significant levels of O atoms and several percent of N atoms at the surface, while in the catalytic case these species have close to zero mass fraction on the surface.

Figure 3 shows that at 60 km, the effect of surface catalysis is somewhat larger than at 40 km, with a 69% increase relative to the noncatalytic heat transfer rate. At 80 km, there is no detectable difference between the catalytic and noncatalytic cases because there are very low levels of dissociation, as shown in the lower right panel.

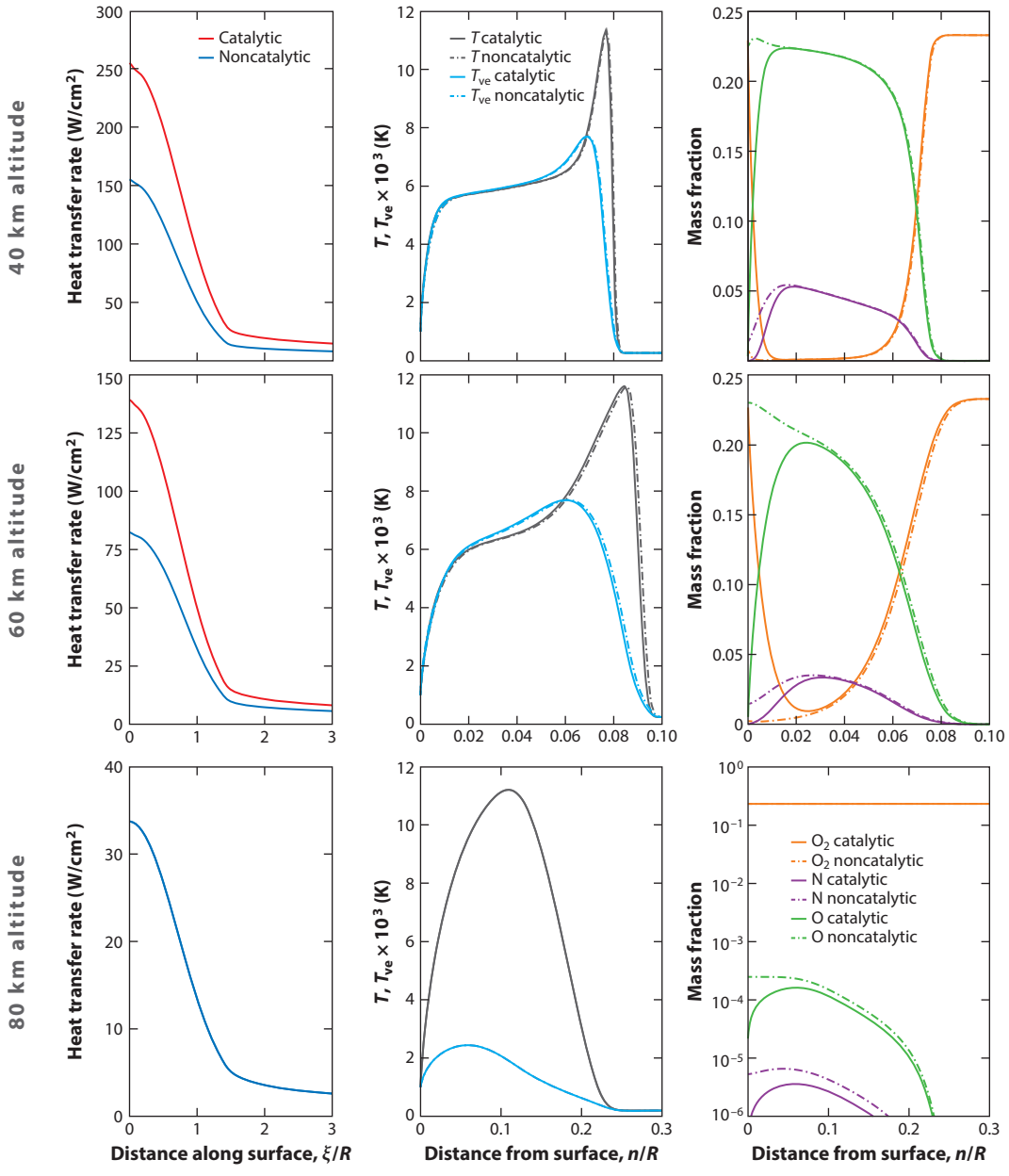

Figure 3

Heat transfer rate to the sphere-cone surface (*left*), the temperature distribution along the stagnation streamline (*center*), and the species mass fraction distribution along the stagnation streamline (*right*) for three altitudes: 40 km, 60 km, and 80 km. Two surface models are used: catalytic, such that all atomic species impacting the surface recombine, and noncatalytic, in which the surface does not promote recombination. Variables: ξ, distance along the surface from the stagnation point; n, the surface-normal distance at the stagnation point.

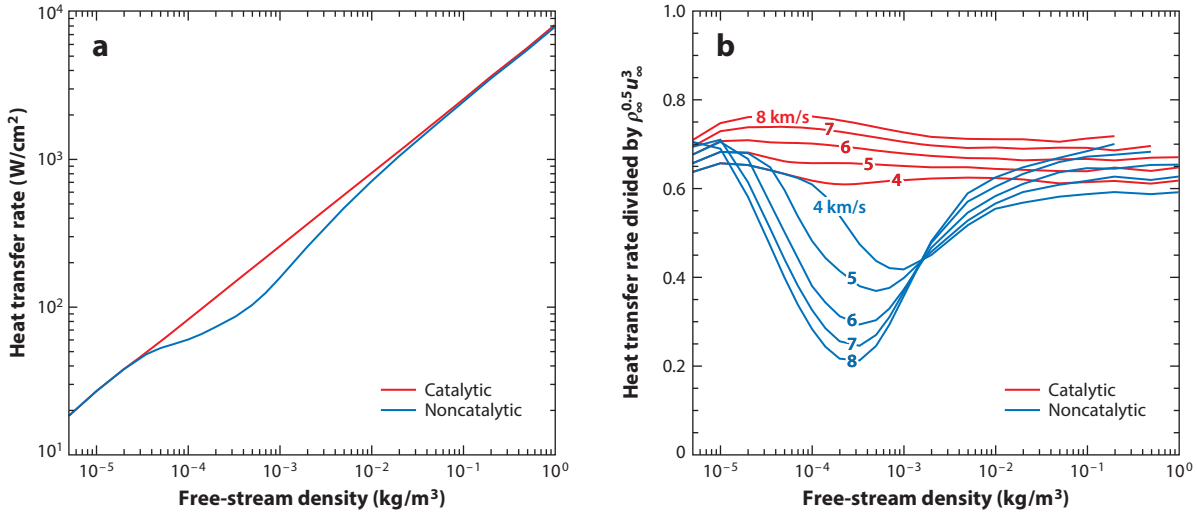

Figure 4

(*a*) Heat transfer rate to the stagnation point of a 10-cm sphere in air at 5 km/s as a function of free-stream density. (*b*) Stagnation-point heat transfer rate normalized by the square root of the free-stream density and free-stream speed cubed, $\sqrt{\rho_\infty} u_\infty^3$, for five free-stream speeds (in meter–kilogram–second units).

Figure 4*a* shows the variation of the stagnation-point heat transfer rate as a function of the free-stream density for the 0.1-m radius sphere at 5 km/s and a surface temperature of 1,000 K. The noncatalytic boundary condition has a large effect on the heat transfer rate at moderate densities, but it has a minimal effect at high and low densities. At low densities, there is little to no dissociation, as shown in the 80 km case discussed above. At high densities, the atomic species recombine in the low-temperature boundary layer, reducing the effect of surface catalysis.

Figure 4*b* summarizes a series of CFD simulations comparing catalytic and noncatalytic boundary conditions at different free-stream conditions. The same sphere-cone is run at speeds ranging from 4 km/s to 8 km/s across a wide range of free-stream densities. The ratio of the assumed wall temperature to the free-stream total temperature is fixed at $T_w/T_o = 0.079$ for all cases. The figure plots the stagnation-point heat transfer rate scaled by $\sqrt{\rho_\infty} u_\infty^3$, which approximately collapses the data (see Tauber et al. 1987). Note that with this scaling, the catalytic surface stagnation-point heat flux is approximately independent of density, while the noncatalytic surface condition shows strong variations over a range of free-stream densities. The largest effect is for the highest speed condition, but even at 4 km/s there is a substantial reduction in the stagnation-point heat flux for densities of about $\rho_\infty \simeq 3 \times 10^{-4}$ kg/m^3. As in **Figure 4*a***, the reduction in heat flux diminishes when the flow is close to chemically frozen (low ρ_∞) and when the near-surface boundary layer is close to chemical equilibrium (high ρ_∞).

These computational results are consistent with the reacting boundary layer theory results of Fay & Riddell (1958), as reproduced in **Figure 5**. The heat transfer coefficient on a flat plate is plotted as a function of the gas-phase recombination rate and the catalytic activity of the surface. The heat flux is shown to be independent of the recombination rate for a catalytic surface and falls off significantly if the surface is noncatalytic and the recombination is slow. This effect was known at the time of the design of the Space Shuttle orbiter, but it was not possible to test the reaction-cured glass tiles at flight conditions, and therefore the conservative fully catalytic heat flux was used to design the thermal protection system. During the early reentries of the orbiter,

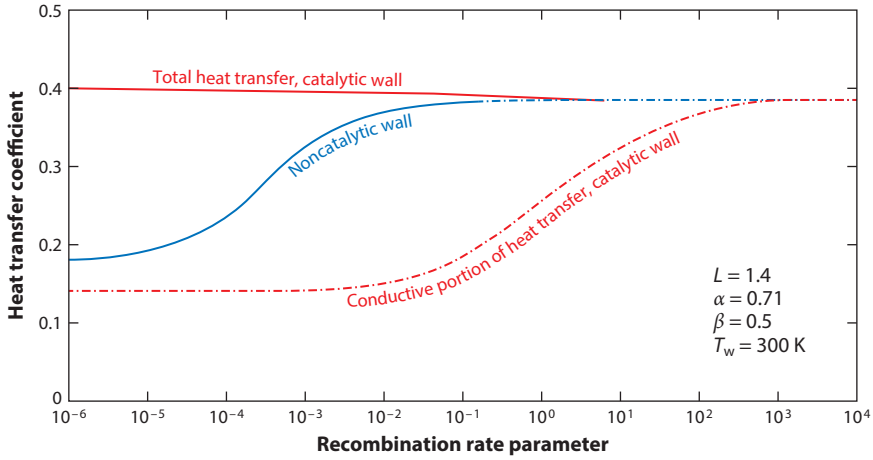

Figure 5

Nondimensional stagnation-point heat transfer rate for a reacting boundary layer with finite recombination rates and limiting values of surface catalytic activity. Adapted with permission from Fay & Riddell (1958).

experiments were performed to assess the catalytic surface effects. Several tiles were coated with a highly catalytic material, and in-flight measurements showed a large heat flux increase on those tiles due to catalytic effects (Stewart et al. 1983, Curry 1993), reflecting the effects shown in **Figures 4** and **5**.

1.3. Effects of Rate Processes on Hypersonic Flight Systems

The examples discussed above illustrate that finite-rate processes can significantly affect hypersonic flows and may result in complex out-of-equilibrium behavior of the gas. In this section, we discuss the effects of rate processes on several flight and ground-test systems.

One of the best known hypersonic rate effects is the Space Shuttle orbiter pitch anomaly. During the first reentry of the orbiter at Mach numbers above 16, the body flap had to be deflected by 16° instead of the predicted 7° in order to trim the vehicle at a 40° angle of attack (Maus et al. 1984, Iliff & Shafer 1993). This discrepancy is typically attributed to so-called real gas effects (Weilmuenster et al. 1994), which refers to imperfect gas or chemical reaction effects. However, this conclusion is not universally accepted in the literature, and the discrepancy has also been attributed to a viscous–inviscid flow interaction (Koppenwallner 1987). This occurs because at hypersonic conditions, boundary layers tend to be thicker than their equivalent–Reynolds number low-speed counterparts. The near-surface shear raises the boundary layer temperature, lowering the density and increasing the viscosity. The resulting thick, highly viscous boundary layer can reduce the effectiveness of control surfaces. The high boundary layer temperatures can also produce finite-rate processes in the boundary layer and on the surface. It is very difficult, if not impossible, to replicate the combination of these effects in ground-test facilities.

The level of chemical reaction has a direct effect on the bow shock standoff distance in hypersonic flows; this can change the pressure distribution and aerodynamic performance of blunt capsules. For example, it was shown that the Mars Pathfinder capsule's aerodynamic stability changes significantly with Mach number and the amount of chemical reaction (Gnoffo et al. 1996). This effect occurs because increasing reaction increases the density rise across the bow

shock, which causes the shock standoff distance to decrease. This in turn changes the location of the sonic line and the resulting pressure distribution on the capsule forebody.

Experiments, theory, and numerical simulations show that finite-rate processes (vibrational relaxation in particular) can affect laminar–turbulent transition in hypersonic boundary layers. For example, Adam & Hornung (1997) and Germain & Hornung (1997) correlated experimental data on a sharp cone as a function of free-stream total enthalpy for air, nitrogen, and carbon dioxide. They showed that reactive CO_2 has a larger transition Reynolds number relative to air, and particularly in contrast to low-reactivity nitrogen. Subsequent theoretical analyses showed that the relaxation of the CO_2 vibrational modes damps instability growth in these flows, resulting in transition delay. This interaction is discussed in more detail in Section 4.2.

Many hypersonic flight vehicles require the use of ablative thermal protection systems, in which the surface material interacts with the external high-temperature flow and undergoes finite-rate gas-surface reactions. These processes include oxidation and nitridation reactions, catalytic recombination, sublimation, and erosion. Ablation results in surface mass loss and the injection of surface reaction products into the flow. The mass injection pushes the boundary layer away from the surface and shields the body from the high-temperature shock-layer gas. The ablation species undergo gas-phase reactions in the boundary layer and wake. Such a thermal protection system is not reusable because the ablation process consumes a portion of the surface material. An example of graphite ablation is given in Section 6.

The operation of many high-enthalpy test facilities is affected by finite-rate processes. For example, shock tunnels are used to generate a short-duration flow to simulate hypersonic flight in the atmosphere. To do so, a shock wave is driven into a quiescent test gas; the shock wave reflects off of the shock tube end wall, producing a slug of high-temperature and -pressure gas. This gas then expands through a converging-diverging nozzle to hypersonic conditions. However, when the test gas is compressed, it undergoes chemical reactions, and it is this reacted gas that expands through the nozzle. Just as the stagnation region gas chemical state is frozen in the sphere-cone flow, the test gas state may freeze during the expansion through the nozzle, resulting in a partially reacted test gas. This gas is at low temperature, but with potentially large mass fractions of atoms and other reaction products. In some cases, particularly N_2 flows, the vibrational energy can also be frozen near the nozzle throat temperature.

2. GOVERNING EQUATIONS

The governing equations and associated boundary conditions for hypersonic flows are discussed in this section. The examples described above show that these flows are not in local thermodynamic equilibrium and that there can be significant effects of rate processes on important flow features. Thus, it is necessary to track the evolution of the thermochemical state of the gas with appropriate conservation equations. The overall form of the governing equations is described; more details may be found in Gnoffo et al. (1989) and Lee (1985), for example.

2.1. Conservation Equations

The evolution of the mass of chemical species s is given by the conservation equation

$$\frac{\partial \rho_s}{\partial t} + \frac{\partial}{\partial x_j}(\rho_s u_j + \rho_s v_{sj}) = \omega_s, \qquad 1.$$

where ρ_s is the species-s density, u_j is the mass-averaged velocity in the x_j direction, v_{sj} is the species-s mass diffusion velocity, and ω_s is the species-s chemical source term.

The momentum conservation equation is

$$\frac{\partial \rho u_i}{\partial t} + \frac{\partial}{\partial x_j}(\rho u_i u_j + p\delta_{ij} - \sigma_{ij}) = 0, \quad 2.$$

where p is the pressure and σ_{ij} is the stress tensor. As discussed above, the internal energy may be out of equilibrium with the translational (thermal) energy in a hypersonic flow. In that case, its evolution is governed by an additional internal energy conservation equation of the form

$$\frac{\partial \rho e_{\text{int}}}{\partial t} + \frac{\partial}{\partial x_j}\left(\rho e_{\text{int}} u_j + \sum_s \rho_s e_{\text{int},s} v_{sj} + q_{\text{int},j}\right) = Q_{\text{int}}, \quad 3.$$

where e_{int} is the mass-averaged internal energy (in the previous examples, e_{int} is the sum of the vibrational and electronic energies), and $q_{\text{int},j}$ is the j-direction energy flux due to gradients of internal energy. The source term, Q_{int}, represents the rate of internal energy relaxation due to collisional processes in the gas mixture. The internal energy e_{int} can be written as

$$\rho e_{\text{int}} = \sum_s \rho_s e_{\text{int},s}, \quad 4.$$

where $e_{\text{int},s}$ is the species-s internal energy. The specific form of $e_{\text{int},s}$ used to represent a particular flow depends on the flow conditions, gas properties, and quantities of interest being simulated. In some cases, multiple internal energy equations must be solved. For example, it may be necessary to track several vibrational energies or to solve a separate electronic energy equation.

Finally, the total energy conservation equation is given by

$$\frac{\partial E}{\partial t} + \frac{\partial}{\partial x_j}\left[(E + p)u_j - \sigma_{ij}u_i + \sum_s \rho_s h_s v_{sj} + q_j\right] = 0, \quad 5.$$

where E is the total energy per unit volume,

$$E = \sum_s \rho_s e_s + \frac{1}{2}\rho u_k u_k. \quad 6.$$

Here, e_s is the species-s total specific energy, including all energy modes (translational, rotational, vibrational, electronic, and chemical):

$$e_s = e_{\text{tr},s} + e_{\text{int},s} + h_s^\circ, \quad 7.$$

where $e_{\text{tr},s}$ is the translational–rotational energy and h_s° is the heat of formation. In the above conservation equation, h_s is the species-s specific enthalpy, $h_s = e_s + p_s/\rho_s$. The pressure is the sum of the partial pressures of the gas mixture.

Unless all scales are resolved, which is currently prohibitive at vehicle scales, these equations must be augmented for turbulent flows, either by adding transport equations for Reynolds-averaged Navier–Stokes turbulence model variables or by including large-eddy simulation subgrid-scale models. The present state of turbulence modeling for hypersonic flows is deficient, and turbulence models developed for low-speed flows are typically used.

2.2. Thermodynamics

It is critical to correctly represent the thermodynamics of high-temperature hypersonic flows. For moderate–Mach number flows, there is little to no electronic excitation, and the vibrational energy modes can be adequately represented with a simple harmonic oscillator. Above about Mach 15 in air, it is important to include electronic energy excitation. This can be done with algebraic expressions for the electronic energy states of each species, utilizing data for energy

levels and degeneracies. However, this can be cumbersome and it is usually preferable to use curve fits for thermodynamic quantities such as those of McBride et al. (2002) and Scoggins & Magin (2014). With a two-temperature model for the translational–rotational and vibrational–electronic energies, care must be taken to correctly evaluate the different energies at the appropriate temperatures.

2.3. Source Terms

Let us consider nitrogen dissociation, written as

$$\mathrm{N_2 + M \rightleftharpoons N + N + M}, \tag{8.}$$

where M represents a collision partner. The law of mass action for the source term, $\omega_{\mathrm{N_2}}$, is

$$\omega_{\mathrm{N_2}} = -M_{\mathrm{N_2}} \left[\frac{\rho_{\mathrm{N_2}}}{M_{\mathrm{N_2}}} \sum_s k_{\mathrm{f},s} \frac{\rho_s}{M_s} - \left(\frac{\rho_{\mathrm{N}}}{M_{\mathrm{N}}} \right)^2 \sum_s k_{\mathrm{b},s} \frac{\rho_s}{M_s} \right]. \tag{9.}$$

M_s is the species-s molecular weight, and $k_{\mathrm{f},s}$ and $k_{\mathrm{b},s}$ are the forward (dissociation) and backward (recombination) reaction rates, respectively. Usually, the dissociation rate is computed from a temperature-dependent Arrhenius reaction rate, and the recombination rate is set so that the source term is zero in thermodynamic equilibrium.

The internal energy relaxation term, Q_{int}, is complicated for ionizing gases and is not discussed in full here; readers are referred to Gnoffo et al. (1989) and Lee (1985) for more details. Rather, we focus on the term that is responsible for vibrational energy relaxation through collisional processes. The standard approach is to use a Landau–Teller model,

$$Q_{\mathrm{v}} = \sum_s \frac{\rho_s e^*_{\mathrm{v},s}(T) - \rho_s e_{\mathrm{v},s}}{\tau_{\mathrm{v},s}} + \sum_s \omega_s \tilde{e}_{\mathrm{v},s}, \tag{10.}$$

where $\tau_{\mathrm{v},s}$ is the species-s translational–vibrational relaxation time that is appropriately averaged to account for different relaxation times for each collision pair. Here, $\tilde{e}_{\mathrm{v},s}$ is the average vibrational energy removed or added to the vibrational energy pool due to dissociation and recombination reactions, respectively. As discussed below, vibrationally excited molecules dissociate more readily, and therefore this value should be larger than the average vibrational energy.

2.4. Transport Properties

Gas transport properties are critical for the accurate representation of high-temperature rate-dependent flows. There are several approaches to computing the transport properties, ranging from the approximate Wilke mixing rule (Wilke 1950) to more accurate representations of the results from kinetic theory (Hirschfelder et al. 1954, Gupta et al. 1990). Seldom is the full multi-component mass diffusion model used because of its cost; rather, the self-consistent effective binary diffusion model (Ramshaw & Chang 1993) is used because of its sufficient accuracy and relatively low cost. For ionized flows, it is critical to accurately compute the Coulombic interactions to obtain the correct overall transport properties. The individual species transport properties are often taken from tabulations of Blottner et al. (1971), Gupta et al. (1990), and Wright et al. (2005), for example.

2.5. Relaxation and Reaction Rates

Hypersonic flows depend on the rates that govern the internal energy relaxation and chemical reaction processes. Until recently, the rates used were primarily based on shock tube data from

the 1960s and 1970s. Standard approaches use Millikan & White's (1963) correlation for the vibrational relaxation times, with some corrections for particular relaxation pairs (Park 1993). A standard set of air reaction rates was tabulated by Park (1993) and, for gas-phase reactions of ablation products, by Martin et al. (2015).

As is discussed in more detail in Section 5, computational chemistry is now providing accurate potential energy surfaces (PESs) that can be used to simulate the reaction dynamics of air species. These are being used to compute more accurate vibrational relaxation times and reaction rates, which are starting to become available in the literature.

2.6. Gas-Surface Boundary Conditions

The surface boundary conditions used for high-enthalpy hypersonic flows are significantly more complicated than the usual no-slip boundary condition used for conventional flows. Here, we provide two examples and refer to appropriate references for more complex boundary conditions.

2.6.1. Catalytic surface boundary condition. The basic statement of mass balance for species s at a reactive surface is given by (MacLean et al. 2011, Marschall & MacLean 2011, Marschall et al. 2015):

$$-(\rho D_s)_\mathrm{w} \left.\frac{\partial y_s}{\partial n}\right|_\mathrm{w} + (\rho u)_\mathrm{w} y_{s\mathrm{w}} = \omega_s. \qquad 11.$$

We have assumed Fickian diffusion; D_s is the mass diffusivity, y_s is the species-s mass fraction, and u is the rate of motion of the surface due to reactive mass loss by the gas-surface reactions with rate ω_s. The w subscript indicates the wall condition. These reactions produce a flux of reacted species to or from the surface, rather than a volumetric rate of mass production, as in the gas-phase reactions.

Let us consider the example of a catalytic surface discussed above. The catalytic efficiency, α, is the fraction of atoms impinging on a surface that undergo reaction (recombine to molecules) on the surface. The surface mediates the recombination process by one of several possible surface reaction processes. From kinetic theory, the one-way flux of species-s particles across a surface is

$$J_s = \frac{1}{4}\rho_s \bar{C}_s, \qquad 12.$$

where $\bar{C}_s$ is the thermal speed of the species-s particles. Of those particles that impact the surface, a fraction α of them recombine and $1-\alpha$ bounce off and do not react. Thus, the rate of production of species-s mass is $\omega_s = \frac{1}{4}\alpha\rho_s \bar{C}_s$ evaluated at the wall state. Within the continuum description, the flux of reacted particles must be equal to the diffusive flux of reactive gas to the surface. This is represented by the above mass balance expression, and therefore we have a boundary condition of the form

$$-(\rho D_s)_\mathrm{w} \left.\frac{\partial y_s}{\partial n}\right|_\mathrm{w} = \frac{1}{4}\alpha\rho_{s,\mathrm{w}}\bar{C}_{s,\mathrm{w}}, \qquad 13.$$

since $u_\mathrm{w} = 0$ (no mass change of the surface) for this catalytic surface reaction. With the assumption that the normal pressure gradient is zero in the boundary layer, we can then solve for the surface or wall state.

Implicit in this formulation is a rate of reaction on the surface. A noncatalytic surface with $\alpha = 0$ has surface reactions that are negligibly slow relative to the diffusion timescales. Likewise, a large catalytic efficiency ($\alpha \to 1$) represents a rapid surface reaction, and the rate of catalytic recombination is limited by the rate of diffusion to the surface. In more complex gas-surface interaction models, there can be competing surface reactions and reactions that depend on surface

coverage (the fraction of surface material bond sites occupied by gas-phase species). Then the gas-surface reaction rates are explicitly temperature- and pressure-dependent, and the law of mass action is used to develop the rate of chemical species formation on the surface (Marschall et al. 2015).

2.6.2. Velocity and temperature slip boundary conditions. The extended form of the Navier–Stokes equations provided above can be derived using a Chapman–Enskog solution of the Boltzmann equation. Conceptually, a first-order perturbation to a Maxwellian velocity distribution is substituted into the Boltzmann equation and appropriate moments are taken. This results in the Navier–Stokes equations with assumptions for linear relationships between stress and strain and between temperature gradients and heat flux. The surface boundary conditions that are consistent with this kinetic theory–based derivation are the so-called slip boundary conditions. It is only in the limit of small mean free path that the conventional no-slip boundary conditions are recovered.

The dependence of the surface state on the mean free path is easy to visualize. For example, consider a rarefied gas with a mean free path, λ. The particles that impinge on the surface originate about a distance λ from the surface, interact with and accommodate to the surface state, and then collide again about λ from the surface. The influence of the surface is then transmitted to the rest of the flow field through subsequent collisions. This region of adjustment to the surface state thus scales with λ.

Maxwell (1879) derived an expression for the velocity slip in the surface-tangent direction as (see also Gupta et al. 1985)

$$u_{\text{slip}} = \frac{2-\sigma}{\sigma}\lambda \left.\frac{\partial u}{\partial n}\right|_{\text{w}}, \tag{14.}$$

where σ is the accommodation coefficient (the fraction of particles that are diffusely reflected), and n is a surface-normal coordinate. Note that the usual no-slip boundary condition is obtained as $\lambda \to 0$.

A similar temperature jump or slip boundary condition for a perfect gas was derived by Kennard (1938) as

$$T_{\text{slip}} - T_{\text{w}} = \frac{2-\alpha_{\text{T}}}{\alpha_{\text{T}}}\frac{2\gamma}{(\gamma+1)}\frac{1}{\text{Pr}}\lambda \left.\frac{\partial T}{\partial n}\right|_{\text{w}}, \tag{15.}$$

where T_{w} is the wall or surface temperature, α_{T} is the thermal accommodation coefficient, γ is the ratio of specific heats, and Pr is the Prandtl number.

Under low-density rarefied conditions, these slip effects may be important, and it has been shown that greatly improved comparisons between particle-based flow simulations [e.g., direct simulation Monte Carlo (Boyd & Schwartzentruber 2017)] and the Navier–Stokes equations are obtained when they are included (Gupta et al. 1985, Gokcen 1989, Lofthouse et al. 2008, Bhide et al. 2018).

An interesting rate-driven example of surface slip effects involves CUBRC shock tunnel experiments, in which moderate-enthalpy N_2 is shock heated and expanded to hypersonic conditions (Nompelis et al. 2003). Due to the rapid expansion of the gas, the vibrational energy freezes close to the nozzle throat conditions. A typical hypersonic test condition has a free-stream translational–rotational temperature of 98 K, while the vibrational temperature is frozen close to the nozzle throat conditions at 2,560 K. To obtain good agreement between numerical simulations and heat transfer measurements in this nonequilibrium test gas, it is necessary to include a vibrational energy slip model with the experimentally measured accommodation coefficient of 10^{-3}.

2.7. Nondimensionalization and Scaling

The chemical source term can be nondimensionalized using the free-stream density, velocity magnitude, and a relevant length scale, L. This results in a nondimensional source term for the N_2 dissociation reaction (Equation 9),

$$\bar{\omega}_{N_2} = \frac{L}{\rho_\infty u_\infty}\omega_{N_2} = -M_{N_2}\left[\frac{\rho_\infty L}{u_\infty}\frac{\bar{\rho}_{N_2}}{M_{N_2}}\sum_s k_{f,s}\frac{\bar{\rho}_s}{M_s} - \frac{\rho_\infty^2 L}{u_\infty}\left(\frac{\bar{\rho}_N}{M_N}\right)^2\sum_s k_{b,s}\frac{\bar{\rho}_s}{M_s}\right], \qquad 16.$$

where the bar variables are nondimensional quantities. Note that the relevant scaling parameters are

$$\text{forward (dissociation) rate:} \quad \frac{\rho_\infty L}{u_\infty}, \qquad 17.$$

$$\text{backward (recombination) rate:} \quad \frac{\rho_\infty^2 L}{u_\infty}. \qquad 18.$$

The dissociation source term scales with the density, while recombination scales with the density squared. Therefore, the relative importance of dissociation and recombination can change as the free-stream density changes. It should also be noted that the flow-field temperature scales with u_∞^2, so that the temperature-dependent rates, k_f and k_b, scale with the free-stream velocity magnitude squared.

Dissociation is a two-body binary collision process, so the $\rho_\infty L$ scaling is termed binary scaling (Hornung 1972b). Other two-body processes such as exchange reactions (e.g., $N_2 + O \rightleftharpoons NO + N$) also have binary scaling. Similarly, the vibrational relaxation process is a two-body process and is characterized by binary scaling (τ_v in Equation 10 scales inversely with density). Recombination is a three-body or ternary process, accounting for its dependence on the density squared.

The flows discussed above clearly exhibit these scaling properties. The rate of dissociation and vibrational relaxation behind the bow shock decreases with decreasing free-stream density, as expected. However, the recombination process exhibits a stronger dependence on density. When the gas suddenly expands around the nose and onto the cone, the density decreases and the rate of recombination decreases quadratically with the density. This is why there is little recombination during the flow expansion and why the chemical freezing is stronger at 60 km than at 40 km. In contrast, because vibrational relaxation is a binary collisional process, it more closely follows the changes in the translational temperature.

A more subtle scaling effect occurs in the near-surface boundary layer. At 40 km, the density is high enough that significant recombination occurs in the thermal boundary layer. However, at 60 km, the density is lower and recombination is reduced due its quadratic dependence on density. This causes the dependence of the noncatalytic heat transfer rate on density shown in **Figure 4**.

The scaling of the gas-surface reactions is not as clear as the gas-phase reactions. For example, consider the catalytic recombination of oxygen according to $O + O(s) \rightarrow O_2$; here, $O(s)$ is an oxygen atom that is bonded to an open surface site. The rate of this process is not simple since it is proportional to both the gas-phase O atom concentration and the number of O atoms bonded to the surface. Typically, the surface coverage depends on the surface temperature and gas pressure.

These rates can be nondimensionalized by a characteristic advection rate, resulting in Damköhler numbers for each process. In the limit of large Damköhler number, a process will be close to equilibrium, while small values indicate that it is frozen.

3. TRANSLATIONAL AND ROTATIONAL PROCESSES

We do not usually think of translational relaxation or thermalization of a gas as a rate process. However, in hypersonic flows, the change of the gas state can be so rapid that the translational

modes are relatively slow to adjust. When this occurs, the fundamental assumptions of the kinetic theory derivation of the Navier–Stokes equations are violated.

An obvious example of translational nonequilibrium occurs within a strong shock wave. The preshock velocity distribution function has a small thermal component and a large component in the free-stream direction. Postshock, the opposite is true, with much of the upstream directed motion converted to thermal motion. Within the shock wave itself, the velocity distribution function is much more complicated, with features of the pre- and postshock distribution functions. Such a bimodal velocity distribution function cannot be represented as a perturbed Maxwellian distribution, as assumed by the Chapman–Enskog derivation of the Navier–Stokes equations. Thus, the Navier–Stokes equations cannot correctly represent the flow within a shock wave. Likewise, higher-order Chapman–Enskog solutions of the Boltzmann equation (e.g., the Burnett equations) cannot represent this effect.

When translational energy relaxation is important, a kinetic theory–based approach such as the direct simulation Monte Carlo method must be used (Bird 1994, Boyd & Schwartzentruber 2017). Typically, this occurs under rarefied conditions, which can be identified using a gradient-length local Knudsen number (Boyd et al. 1995):

$$\mathrm{Kn}_{\mathrm{GLL}} = \frac{\lambda}{\rho}\|\nabla\rho\|. \qquad 19.$$

If this quantity exceeds a value of about 0.05, the Navier–Stokes equations are likely to be invalid.

Typically, rotational energy relaxation does not need to be considered separately since it is only important for flows where the Navier–Stokes equations are already suspect or invalid. This is because the rotational modes relax very rapidly (in about five to ten collisions), and that rate is similar to the rate at which the translational modes relax to equilibrium. This is not the case for the vibrational modes.

4. VIBRATIONAL PROCESSES

The relatively slow relaxation of the vibrational modes of a gas can interact with the gas dynamics in several ways. Most obviously, the vibrational modes absorb energy and change the postshock conditions when they are active. The vibrational state of the gas also has a strong effect on its dissociation rate, as discussed in the next section. Vibrational freezing and thermal nonequilibrium can be important in rapidly expanding flows such as in the wake of a planetary entry capsule or in a hypersonic wind tunnel nozzle, as shown above. In some flows, the vibrational relaxation rate may be tuned to match acoustic disturbances, which can lead to the dissipation and dispersion of sound in high-temperature gases. Acoustic damping by this mechanism can counter boundary layer instabilities and delay transition to turbulence if tuned to the dominant instabilities. In this section, we summarize the interaction of vibrational relaxation with acoustic processes.

4.1. Vibrational Relaxation and the Bulk Viscosity

The derivation of the stress tensor for a linearly viscous fluid yields

$$\sigma_{ij} = -p\delta_{ij} + \mu_{\mathrm{B}}\,\delta_{ij}\nabla\cdot\mathbf{u} + \mu\left(\frac{\partial u_i}{\partial x_j} + \frac{\partial u_j}{\partial x_i} - \frac{2}{3}\delta_{ij}\nabla\cdot\mathbf{u}\right), \qquad 20.$$

where μ_{B} is the bulk viscosity (e.g., Thompson 1988); the same result can be obtained from kinetic theory (Hirschfelder et al. 1954). Deviations of the average normal stress from the pressure are commonly ascribed to nonzero values of μ_{B} (Emanuel 1992); nonzero μ_{B} also has an effect on the

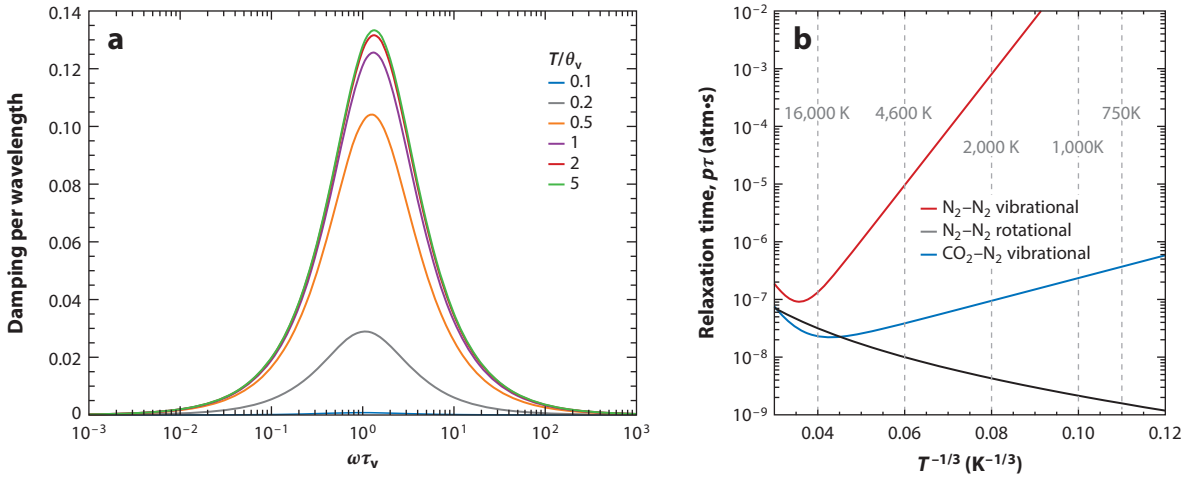

Figure 6

(*a*) Vibrational damping rate as a function of the product of the angular frequency and relaxation time, $\omega\tau_v$, from the results of Meador et al. (1996), and (*b*) typical vibrational and rotational relaxation times. θ_v is the molecular characteristic temperature of vibration.

speed of sound and its attenuation. However, Meador et al. (1996) showed that μ_B is zero and that its interpretation as an internal energy relaxation parameter is incorrect. Rather, absorption and dispersion of sound are the result of internal energy relaxation, but these effects are not embodied in μ_B. Instead, the internal energy should be represented with a conservation equation, as discussed in Section 2.1. Meador et al. also derived closed-form expressions for the speed of sound and its dissipation rate and dispersion as functions of the internal energy relaxation time.

Figure 6*a* shows the damping rate of acoustic waves as a function of the acoustic angular frequency times the relaxation time, $\omega\tau_v$, and the damping of the acoustic wave per wavelength (Meador et al. 1996). Clearly, $\omega\tau_v \simeq 1$ produces significant damping, provided that the temperature is large enough that the vibrational modes are excited. Here, θ_v is the characteristic temperature of vibration, which is 3,395 K for N_2 and 2,239 K for O_2. **Figure 6*b*** shows that the relaxation times for vibrational and rotational processes vary widely. Therefore, to obtain effective damping, the relaxation process must be resonant with the acoustic frequency of interest. The next section discusses how this effect may be used to damp instabilities in a hypersonic boundary layer.

4.2. Effect of Vibrational Processes on Boundary Layer Stability

During the late 1990s, experiments on a sharp 5° cone in the California Institute of Technology T5 free-piston shock tunnel showed that boundary layer transition depends on the free-stream total enthalpy and the gas properties (Adam 1997, Adam & Hornung 1997, Germain & Hornung 1997). As shown in **Figure 7*a***, the transition Reynolds number based on the boundary layer reference temperature increases with increasing total enthalpy, and thereby with increasing internal energy excitation and chemical reaction. In addition, the transition Reynolds number is an order of magnitude larger in CO_2 than it is in air or N_2. At these conditions, boundary layer transition occurs via the Mack second mode (Mack 1975), which is an acoustic disturbance in the boundary layer.

Linear stability theory at the T5 conditions shows that under certain conditions, vibrational energy relaxation and chemical reactions result in reduced instability growth rates. Furthermore, numerical experiments show that exothermic (heat-releasing) finite-rate processes increase the

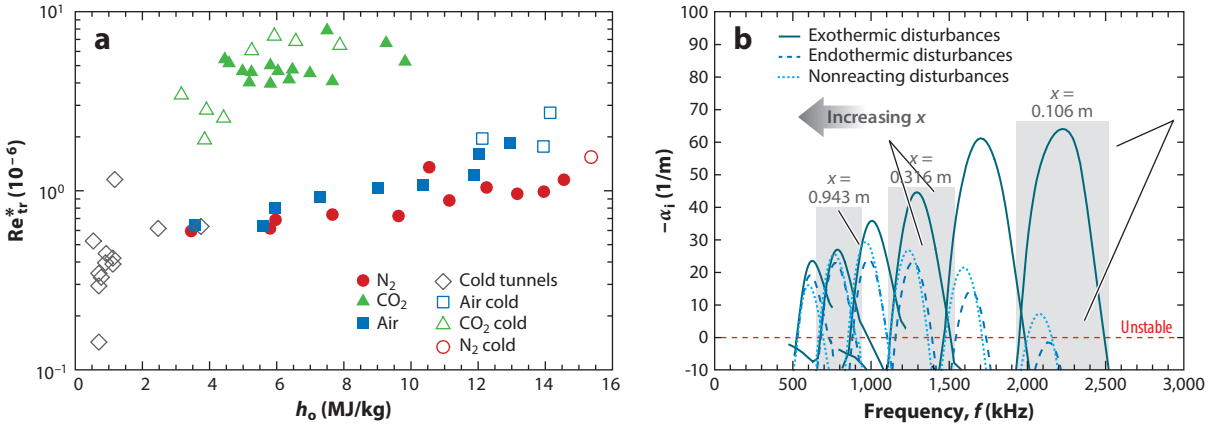

Figure 7

(*a*) The transition Reynolds number based on reference conditions, Re^*_{tr}, on a 5° cone as a function of free-stream total enthalpy, h_o, for three gases. (*b*) The acoustic disturbance growth rate, $-\alpha_i$, at various axial locations on a sharp cone in CO_2 for disturbances with exothermic reactions, endothermic reactions, and no reactions. Panels adapted with permission from (*a*) Adam (1997) and (*b*) Johnson (2000).

growth rate, while endothermic processes decrease it. This demonstrates that there can be an interaction between rate processes and the growth of second-mode disturbances in a hypersonic boundary layer. **Figure 7*b*** summarizes the linear stability theory results. The exothermic reactions are significantly more unstable, while the endothermic reactions are damped relative to the nonreacting flow.

Fujii & Hornung (2001) showed that at the experimental conditions, there is an overlap between the most unstable acoustic frequencies and the vibrational relaxation rate of CO_2. Their work shows that if boundary layer instabilities are tuned to CO_2 relaxation, their amplitude may be damped. Based on this work, Leyva et al. (2009) and Jewell et al. (2013) studied the injection of CO_2 into the boundary layer of a hypersonic cone in an attempt to delay transition to turbulence. With careful injection, it was shown that it is possible to stabilize the boundary layer.

Wagnild & Candler (2014) used direct numerical simulations to study the tuning of acoustic disturbances to hypersonic boundary layers. The results of this work are consistent with the theoretical results and illustrate the effects of vibrational relaxation tuning on acoustic disturbances. There have been many other studies of hypersonic boundary layers including rate effects; however, there are very few that focus on vibrational rate processes and their interaction with the acoustic modes (e.g., Hudson et al. 1997, Knisely & Zhong 2018). Many other authors have studied the effects of equilibrium gas models and chemical nonequilibrium processes. However, chemical rate processes are much slower than the relevant disturbances in hypersonic boundary layers and are not tuned to relevant disturbance frequencies.

This work shows that there are three regimes for vibrational damping of acoustic waves: (*a*) equilibrium, in which the vibrational state rapidly adjusts to the acoustic disturbance (this occurs at low frequencies); (*b*) nonequilibrium, when the vibrational mode responds to the passage of the acoustic disturbance with a phase lag, which absorbs energy from the acoustic mode; and (*c*) frozen, in which the acoustic timescale is much smaller than the vibrational relaxation timescale and does not respond to the passage of the wave, so that there is negligible acoustic damping.

Figure 8 illustrates these regimes for a 100-kHz acoustic wave passing through CO_2 at a range of initial temperatures. At low temperature (300 K), the acoustic modes are only weakly excited, and the relaxation time is much slower than the characteristic time of the acoustic wave. Thus,

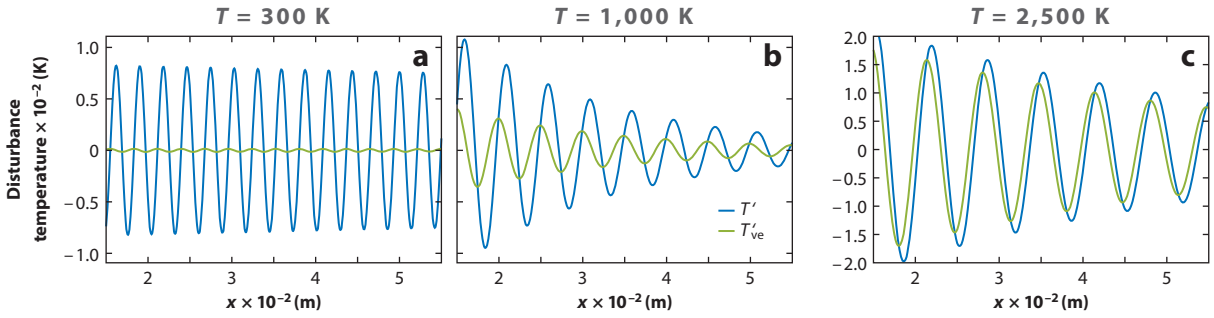

Figure 8

Damping of a 100-kHz acoustic disturbance in CO_2 as a function of temperature: (*a*) 300 K, (*b*) 1,000 K, and (*c*) 2,500 K. Adapted from Wagnild & Candler (2014) with permission from the authors.

the vibrational modes do not respond and are frozen. This is the case in room-temperature air, for example. At 1,000 K, the bending modes of CO_2 are excited ($\theta_v = 960$ K) and their relaxation times are close to the optimal frequency for acoustic damping. In this case, the vibrational energy is excited and its response is out of phase with the translational–rotational temperature; this results in strong acoustic damping. At higher temperatures, the vibrational energy approaches equilibrium and rapidly responds to the temperature perturbations caused by the acoustic wave.

5. CHEMICAL REACTIONS

As illustrated in the introduction, dissociation is an important process in hypersonic flows. Dissociation is complicated because its rate depends on the level of vibrational excitation; vibrationally excited molecules have a lower energy barrier to dissociation and more readily dissociate. Furthermore, when vibrationally excited molecules dissociate, they are removed from the vibrational energy pool, suppressing the overall vibrational energy of the gas mixture. The coupling between vibration and dissociation has been known since the 1960s, and models were postulated to represent the process (e.g., Marrone & Treanor 1963). These models make the effective dissociation rate a function of T and T_v.

In the late 1980s, Park (1986, 1987) recognized that a new approach was needed. The dissociation rates used in flow field modeling were obtained from shock tube experiments, and models were required to infer the reaction rates from the raw data. Park reinterpreted the shock tube data to calibrate a model in a form that would be consistent with the data. This was an important advance over previous models that took the reaction rates as given and then developed models for dissociation. Such an approach is inconsistent because the inferred reaction rates depend on the model used to infer them. Park's analysis resulted in the $\sqrt{TT_v}$ model, in which reaction rates in Arrhenius form are evaluated at an effective temperature equal to $\sqrt{TT_v}$. The model suppresses the dissociation rate when T_v is low, consistent with the understanding of the dissociation process (e.g., Hornung 1972a). A component of this model is the average energy removed from the total vibrational energy due to dissociation ($\tilde{e}_{v,s}$ in Equation 10). Park assumed $\tilde{e}_{v,s} = 0.3\,D_e$, where D_e is the dissociation energy of the molecule. This value is incorrect and causes numerical problems, and in practice, $\tilde{e}_{v,s}$ is typically approximated as the average vibrational energy. The Park model is now widely used, not because it has proven to be accurate, but because it is more straightforward to implement than many other models. Subsequently, other models have been proposed (e.g., Knab et al. 1995, Luo et al. 2018, Singh & Schwartzentruber 2018).

Recently, it has become possible to better understand the dissociation process through the use of ab initio computational chemistry methods. Electronic-structure calculations are carried out for many possible atomic configurations to build a PES for molecular interactions (e.g., Paukku et al. 2013). Collisions between air species are simulated using the relevant PES to obtain statistical data for relaxation and reaction rates at specified conditions (e.g., Bender et al. 2015, Valentini et al. 2016). Such an analysis reveals the complete physics of dissociation and its dependence on the vibrational energy state. Soon this work will supplant Park's $\sqrt{TT_v}$ model with physics-based models of known fidelity. There are many recent papers related to this subject, including those of Kim & Boyd (2013), Panesi et al. (2014), Andrienko & Boyd (2016), Schwartzentruber et al. (2017), and Macdonald et al. (2018).

6. SURFACE PROCESSES

As discussed in the introduction, gas-surface rate processes can have a profound effect on heat transfer rates to hypersonic vehicles. Ablation is significantly more complicated than surface-catalyzed recombination. The simplest ablative surface is carbon in one form or another, such as graphite or a carbon–carbon matrix. The basic reactions that can take place are oxidation and nitridation, surface-catalyzed recombination, and at high temperatures, sublimation. A representative gas-surface kinetics model is (Zhluktov & Abe 1999)

$$
\begin{aligned}
\mathrm{O} + (s) &\leftrightarrow \mathrm{O}(s), & \mathrm{O}(s) + \mathrm{C}(b) &\leftrightarrow \mathrm{CO} + (s),\\
\mathrm{N} + (s) &\leftrightarrow \mathrm{N}(s), & \mathrm{O} + \mathrm{O}(s) + \mathrm{C}(b) &\leftrightarrow \mathrm{CO_2} + (s),\\
2\mathrm{O}(s) &\leftrightarrow \mathrm{O_2} + 2(s), & 2\mathrm{O}(s) + \mathrm{C}(b) &\leftrightarrow \mathrm{CO_2} + 2(s),\\
\mathrm{O_2} + (s) &\leftrightarrow \mathrm{O} + \mathrm{O}(s), & \mathrm{C} + (s) &\leftrightarrow (s) + \mathrm{C}(b),\\
\mathrm{N_2} + (s) &\leftrightarrow \mathrm{N} + \mathrm{N}(s), & \mathrm{C_2} + 2(s) &\leftrightarrow 2(s) + 2\mathrm{C}(b),\\
\mathrm{CO_2} + (s) &\leftrightarrow \mathrm{CO} + \mathrm{O}(s), & \mathrm{C_3} + 3(s) &\leftrightarrow 3(s) + 3\mathrm{C}(b).
\end{aligned}
$$

Here, (s) indicates an open bond site, $\mathrm{O}(s)$ denotes an O atom occupying a bond site, and $\mathrm{C}(b)$ indicates a bulk or solid carbon atom. Rates for each of these processes are required to close the model.

Until recently, such a finite-rate model was not used for analysis, and a gas-surface equilibrium approximation was made. In this case, the equilibrium composition of a mixture of air and the surface material is computed at the surface pressure and temperature; this provides the surface state for the gas-phase boundary condition. This approach is commonly termed a B' method (the nondimensional mass blowing rate) and is valid at high pressures where equilibrium is approached, but is unlikely to be valid at low to moderate pressures.

Figure 9 shows CFD simulations of ablation using three models: the equilibrium B' approach, Zhluktov & Abe's (1999) finite-rate model, and a recently developed finite-rate model (Poovathingal et al. 2017). The main difference between the finite-rate models is that the more recent model favors the formation of CO relative to CO_2; this is consistent with oxygen molecular beam experiments (Murray et al. 2015). Here, the properties of graphite are used, and the gas-surface mass and energy balances are solved at the interface between the gas and the solid. The thermal response of the material is included, and the body changes shape due to ablative mass loss. Clearly, there are large differences between the models, with the equilibrium B' model producing much larger recession relative to the finite-rate models. The Zhluktov & Abe (1999) model produces the lowest level of recession. Experiments (Alba et al. 2016) indicate that this model is deficient, and the third model is more consistent with data. In any case, it is clear that the finite-rate models produce significantly reduced levels of surface recession at these conditions. Furthermore, the boundary layer composition predicted by the models is completely different,

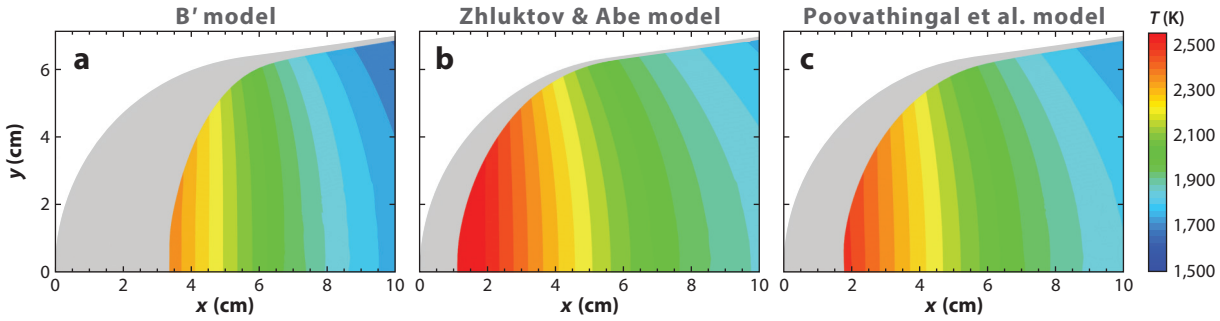

Figure 9

Predicted recession and solid temperature for a graphite sphere-cone (6.35 cm in radius) at conditions corresponding to an altitude of 30 km and a flight speed of 3.5 km/s after 830 s of exposure: (*a*) B' model, (*b*) Zhluktov & Abe (1999) model, and (*c*) Poovathingal et al. (2017) model. The gray region indicates the initial preablated geometry.

and as shown in Section 4.2, the boundary layer internal energy dynamics can lead to important effects. Additional experimental data are required to fully validate the models.

SUMMARY POINTS

1. Hypersonic flows involve interactions of gases and thermal protection system materials at extreme conditions.
2. In hypersonic flows, internal energy relaxation, gas-phase reactions, and gas-surface interactions typically occur at rates that are similar to the gas motion rates, resulting in an out-of-equilibrium thermochemical state.
3. These rate processes affect aerodynamic performance, heat transfer rates, instability growth leading to boundary layer transition, catalytic gas-surface interactions, and ablation.
4. Hypersonic flows are sensitive to the scaling of the chemical rate processes, with dissociation governed by binary scaling and recombination by ternary scaling.
5. Advanced multiphysics simulations and computational chemistry methods are being used to understand and accurately model key rate processes.

FUTURE ISSUES

1. Validation of hypersonic flow simulations and the underlying models remains a critical issue. It is difficult to reproduce all relevant rate processes in ground-based wind tunnels, and making nonintrusive measurements in these flows is a challenge.
2. Advanced simulations should be used to design experiments that target modeling uncertainties and that can be performed in existing wind tunnels.
3. Progress has been made in the development of finite-rate models for graphite ablation, but much work is needed to represent the interaction of more complex thermal protection materials with air reaction products.

4. Little effort has been directed toward understanding turbulent motion at the extreme conditions of hypersonic flight.
5. The prediction of hypersonic rate-dependent flows relies on computational fluid dynamics methods, which have been adapted from methods designed for lower-speed flows. Improved numerical methods need to be developed that are less sensitive to grid imperfections, have low levels of dissipation and yet can capture strong discontinuities, and are efficient for problems with many chemical species and stiff source terms.
6. The high-fidelity simulation of the hypersonic flow environment is far from complete; a hypersonic flight system changes during flight over a large range of time scales. Relevant processes include thermal expansion, material degradation and shape change, surface roughness changes, and fluid–structure interactions and vibrations.

DISCLOSURE STATEMENT

The author is not aware of any biases that might be perceived as affecting the objectivity of this review.

ACKNOWLEDGMENTS

This work was sponsored by the Air Force Office of Scientific Research (AFOSR) under grants FA9550-16-1-0161, FA9550-17-1-0057, and FA9550-17-1-0250. The views and conclusions contained herein are those of the author and should not be interpreted as necessarily representing the official policies or endorsements, either expressed or implied, of the AFOSR or the US Government. The author would like to thank Joseph Brock, Ross Chaudhry, Ioannis Nompelis, and Thomas Schwartzentruber for helpful comments.

LITERATURE CITED

Adam PH. 1997. *Enthalpy effects on hypervelocity boundary layers*. Ph.D. Thesis, Calif. Inst. Technol., Pasadena, CA

Adam PH, Hornung HG. 1997. Enthalpy effects on hypervelocity boundary-layer transition: ground test and flight data. *J. Spacecr. Rockets* 34(5):614–19

Alba CR, Greendyke RB, Lewis SW, Morgan RG, McIntyre TJ. 2016. Numerical modeling of Earth reentry flow with surface ablation. *J. Spacecr. Rockets* 53(1):84–97

Andrienko DA, Boyd ID. 2016. Kinetic models of oxygen thermochemistry based on quasi-classical trajectory analysis. *J. Thermophys. Heat Trans.* 30. **https://doi.org/10.2514/1.T4968**

Bender J, Valentini P, Nompelis I, Paukku Y, Varga Z, et al. 2015. An improved potential energy surface and multi-temperature quasiclassical trajectory calculations of $N_2 + N_2$ dissociation reactions. *J. Chem. Phys.* 143(5):054304

Bhide PM, Singh N, Schwartzentruber TE, Nompelis I, Candler GV. 2018. *Slip effects in near continuum hypersonic flow over canonical geometries*. Paper presented at AIAA Aerospace Sciences Meeting, 56th, Kissimmee, FL, AIAA Pap. 2018-1235

Bird GA. 1994. *Molecular Gas Dynamics and the Direct Simulation of Gas Flows*. Oxford: Oxford Univ. Press

Blottner FG, Johnson M, Ellis M. 1971. *Chemically reacting viscous flow program for multi-component gas mixtures*. Tech. Rep. SC-RR-70-754, Sandia Lab., Albuquerque, NM

Boyd ID, Chen G, Candler GV. 1995. Predicting failure of the continuum fluid equations in transitional hypersonic flows. *Phys. Fluids* 7(1):210–19

Boyd ID, Schwartzentruber TE. 2017. *Nonequilibrium Gas Dynamics and Molecular Simulation*. Cambridge, UK: Cambridge Univ. Press

Candler GV, Johnson HB, Nompelis I, Subbareddy PK, Drayna TW, et al. 2015. *Development of the US3D code for advanced compressible and reacting flow simulations*. Paper presented at AIAA Aerospace Sciences Meeting, 53rd, Kissimmee, FL, AIAA Pap. 2015-1893

Candler GV, Subbareddy PK, Brock JM. 2014. Advances in computational fluid dynamics methods for hypersonic flows. *J. Spacecr. Rockets* 52(1):17–28

Curry DM. 1993. *Space Shuttle Orbiter Thermal Protection System design and flight experience*. NASA Tech. Memo. 104773, Natl. Aeronaut. Space Admin., Washington, DC

Emanuel G. 1992. Effect of bulk viscosity on a hypersonic boundary layer. *Phys. Fluids A* 4(3):491–95

Fay JA, Riddell FR. 1958. Theory of stagnation point heat transfer in dissociated air. *J. Aerosp. Sci.* 25(2):73–85

Fujii K, Hornung HG. 2001. *A procedure to estimate the absorption rate of sound propagating through high temperature gas*. Tech. Rep. 2001-004, GALCIT-FM (Grad. Aerosp. Lab. Calif. Inst. Technol.—Fluid Mech.), Pasedena, CA

Germain P, Hornung HG. 1997. Transition on a slender cone in hypervelocity flow. *Exp. Fluids* 22(3):183–90

Gnoffo PA. 1999. Planetary-entry gas dynamics. *Annu. Rev. Fluid Mech.* 31(1):459–94

Gnoffo PA, Gupta RN, Shinn J. 1989. *Conservation equations and physical models for hypersonic air flows in thermal and chemical nonequilibrium*. NASA Tech. Pap. 2867, Natl. Aeronaut. Space Admin., Washington, DC

Gnoffo PA, Weilmuenster KJ, Braun RD, Cruz CI. 1996. Influence of sonic-line location on Mars Pathfinder probe aerothermodynamics. *J. Spacecr. Rockets* 33(2):169–77

Gokcen T. 1989. *Computation of hypersonic low density flows with thermochemical nonequilibrium*. PhD Thesis, Stanford Univ.

Gupta RN, Scott CD, Moss JN. 1985. *Slip boundary equations for multicomponent nonequilibrium airflow*. NASA Tech. Pap. 2452, Natl. Aeronaut. Space Admin., Washington, DC

Gupta RN, Yos JM, Thompson RA, Lee KP. 1990. *A review of reaction rates and thermodynamic and transport properties for an 11-species air model for chemical and thermal nonequilibrium calculations to 30,000 K*. NASA Ref. Pub. 1232, Natl. Aeronaut. Space Admin., Washington, DC

Hirschfelder O, Curtiss CF, Bird RB. 1954. *Molecular Theory of Gases and Liquids*. New York: Wiley

Hornung HG. 1972a. Induction time for nitrogen dissociation. *J. Chem. Phys.* 56(6):3172–73

Hornung HG. 1972b. Non-equilibrium dissociating nitrogen flow over spheres and circular cylinders. *J. Fluid Mech.* 53(1):149–76

Hudson ML, Chokani N, Candler GV. 1997. Linear stability of hypersonic flow in thermochemical nonequilibrium. *AIAA J.* 35:958–64

Iliff KW, Shafer MF. 1993. *Space Shuttle hypersonic aerodynamic and aerothermodynamic flight research and the comparison to ground test results*. NASA Tech. Memo. 4499, Natl. Aeronaut. Space Admin., Washington, DC

Jewell J, Wagnild R, Leyva IA, Candler GV, Shepherd J. 2013. *Transition within a hypervelocity boundary layer on a 5-degree half-angle cone in air/CO_2 mixtures*. Paper presented at AIAA Aerospace Sciences Meeting, 51st, Grapevine, TX, AIAA Pap. 2013-0523

Johnson HB. 2000. *Thermochemical interactions in hypersonic boundary layer stability*. Ph.D. Thesis, Univ. Minn., Minneapolis, MN

Kennard EH. 1938. *Kinetic Theory of Gases*. New York: McGraw-Hill

Kim JG, Boyd ID. 2013. State-resolved master equation analysis of thermochemical nonequilibrium of nitrogen. *Chem. Phys.* 415:237–46

Knab O, Frühauf H-H, Messerschmid EW. 1995. Theory and validation of the physically consistent vibration-chemistry-vibration model. *J. Thermophys. Heat Transf.* 9(2):219–26

Knisely CP, Zhong X. 2018. *Supersonic modes in hot-wall hypersonic boundary layers with thermochemical nonequilibrium effects*. Paper presented at AIAA Aerospace Sciences Meeting, Kissimmee, FL, AIAA Pap. 2018-2085

Koppenwallner G. 1987. Low Reynolds number influence on aerodynamic performance of hypersonic lifting vehicles. In *AGARD Conference Proceedings, No. 428, Aerodynamics of Hypersonic Lifting Vehicles*, Pap. 11. Neuilly-sur-Seine, Fr.: Advis. Group Aerosp. Res. Dev.

Lee JH. 1985. Basic governing equations for the flight regimes of aeroassisted orbital transfer vehicles. In *Thermal Design of Aeroassisted Orbital Transfer Vehicles*, ed. HF Nelson, pp. 3–53. Reston, VA: Am. Inst. Astronaut. Aeronaut.

Leyva IA. 2017. The relentless pursuit of hypersonic flight. *Phys. Today* 70:30–36

Leyva IA, Laurence S, Beierholm AW-K, Hornung HG, Wagnild W, Candler GV. 2009. *Transition delay in hypervelocity boundary layers by means of CO_2/acoustic instability interactions*. Paper presented at AIAA Aerospace Sciences Meeting, 47th, Orlando, FL, AIAA Pap. 2009-1287

Lofthouse AJ, Scalabrin LC, Boyd ID. 2008. Velocity slip and temperature jump in hypersonic aerothermodynamics. *J. Thermophys. Heat Trans.* 22(1):38–49

Luo H, Alexeenko AA, Macheret SO. 2018. Assessment of classical impulsive models of dissociation in thermochemical nonequilibrium. *J. Thermophys. Heat Transf.* In press

Macdonald RL, Jaffe RL, Schwenke DW, Panesi M. 2018. Construction of a coarse-grain quasi-classical trajectory method. I. Theory and application to N_2–N_2 system. *J. Chem. Phys.* 148(5):054309

Mack LM. 1975. Linear stability theory and the problem of supersonic boundary-layer transition. *AIAA J.* 13(3):278–89

MacLean M, Marschall J, Driver DM. 2011. *Finite-rate surface chemistry model, II: coupling to viscous Navier-Stokes code*. Paper presented at AIAA Thermophys. Conf., 42nd, Honolulu, HI, AIAA Pap. 2011-3784

Marrone PV, Treanor CE. 1963. Chemical relaxation with preferential dissociation from excited vibrational levels. *Phys. Fluids* 6(9):1215–21

Marschall J, MacLean M. 2011. *Finite-rate surface chemistry model, I: formulation and reaction system examples*. Paper presented at AIAA Thermophys. Conf., 42nd, Honolulu, HI, AIAA Pap. 2011-3783

Marschall J, MacLean M, Norman PE, Schwartzentruber TE. 2015. Surface chemistry in non-equilibrium flows. In *Hypersonic Nonequilibrium Flows: Fundamentals and Recent Advances*, ed. E Josyula, pp. 239–327. Reston, VA: Am. Inst. Astronaut. Aeronaut.

Martin A, Cozmuta I, Wright MJ, Boyd ID. 2015. Kinetic rates for gas-phase chemistry of phenolic-based carbon ablator in atmospheric air. *J. Thermophys. Heat Transf.* 29:222–40

Maus JR, Griffith BJ, Szema KY. 1984. Hypersonic Mach number and real gas effects on Space Shuttle Orbiter aerodynamics. *J. Spacecr. Rockets* 21:136–41

Maxwell JC. 1879. *The Scientific Papers of J.C. Maxwell*. New York: Dover

McBride BJ, Zehe MJ, Gordon S. 2002. *NASA Glenn coefficients for calculating thermodynamic properties of individual species*. NASA Tech. Pap. 211556, Natl. Aeronaut. Space Admin., Washington, DC

Meador WE, Miner GA, Townsend LW. 1996. Bulk viscosity as a relaxation parameter: Fact or fiction? *Phys. Fluids* 8:258–61

Millikan RC, White DR. 1963. Systematics of vibrational relaxation. *J. Chem. Phys.* 39:3209–13

Murray VJ, Marshall BC, Woodburn PJ, Minton TK. 2015. Inelastic and reactive scattering dynamics of hyperthermal O and O_2 on hot vitreous carbon surfaces. *J. Phys. Chem. C* 119(26):14780–96

Nompelis I, Candler GV, Holden MS. 2003. Effect of vibrational nonequilibrium on hypersonic double-cone experiments. *AIAA J.* 41(11):2162–69

Panesi M, Munafò A, Magin TE, Jaffe RL. 2014. Nonequilibrium shock-heated nitrogen flows using a rovibrational state-to-state method. *Phys. Rev. E* 90(1):013009

Park C. 1986. *Assessment of two-temperature kinetic model for dissociating and weakly ionizing nitrogen*. Paper presented at AIAA/ASME Jt. Thermophys. Heat Transf. Conf., 4th, Boston, AIAA Pap. 86-1347

Park C. 1987. *Assessment of two-temperature kinetic model for ionizing air*. Paper presented at AIAA Thermophys. Conf., 22nd, Honolulu, HI, AIAA Pap. 87-1574

Park C. 1993. Review of chemical-kinetic problems of future NASA missions, I: Earth entries. *J. Thermophys. Heat Transf.* 7(3):385–98

Paukku Y, Yang KR, Varga Z, Truhlar DG. 2013. Global *ab initio* ground-state potential energy surface of N4. *J. Chem. Phys.* 139(4):044309

Poovathingal S, Schwartzentruber TE, Murray VJ, Minton TK, Candler GV. 2017. Finite-rate oxidation model for carbon surfaces from molecular beam experiments. *AIAA J.* 55(5):1644–58

Ramshaw JD, Chang CH. 1993. Ambipolar diffusion in two-temperature multicomponent plasmas. *Plasma Chem. Plasma Process.* 13(3):489–98

Schwartzentruber TE, Grover MS, Valentini P. 2017. Direct molecular simulation of nonequilibrium dilute gases. *J. Thermophys. Heat Transf.* In press

Scoggins JB, Magin TE. 2014. *Development of Mutation^{++}: multicomponent thermodynamic and transport properties for ionized plasmas written in C^{++}*. Paper presented at AIAA/ASME Jt. Thermophys. Heat Transf. Conf., 11th, Atlanta, GA, AIAA Pap. 2014-2966

Singh N, Schwartzentruber TE. 2018. Non-equilibrium internal energy distributions during dissociation. *PNAS* 115(1):47–52

Stewart DA, Rakich JV, Lanfranco MJ. 1983. Catalytic surface effects on Space Shuttle thermal protection system during Earth entry of flights STS-2 through STS-5. In *Shuttle Performance: Lessons Learned*, pp. 827–45. Washington, DC: Natl. Aeronaut. Space Admin.

Tauber ME, Menees GP, Adelman HG. 1987. Aerothermodynamics of transatmospheric vehicles. *J. Aircraft* 24:594–602

Thompson PA. 1988. *Compressible-Fluid Dynamics*. Troy, NY: Rensselaer Polytech. Inst. Press

Urzay J. 2018. Supersonic combustion in air-breathing propulsion systems for hypersonic flight. *Annu. Rev. Fluid Mech.* 50:593–627

Valentini P, Schwartzentruber TE, Bender JD, Candler GV. 2016. Dynamics of nitrogen dissociation from direct molecular simulation. *Phys. Rev. Fluids* 1(4):043402

Wagnild R, Candler GV. 2014. Computational verification of acoustic damping in high-enthalpy environments. *AIAA J.* 52(11):2615–18

Weilmuenster K, Gnoffo PA, Greene F. 1994. Navier-Stokes simulations of the Shuttle Orbiter aerodynamic characteristics with emphasis on pitch trim and body flap. *J. Spacecr. Rockets* 31(3):355–66

Wilke CR. 1950. A viscosity equation for gas mixtures. *J. Chem. Phys.* 18:517–19

Wright MJ, Bose D, Palmer GE, Levin E. 2005. Recommended collision integrals for transport property computations part 1: air species. *AIAA J.* 43(12):2558–64

Zhluktov SV, Abe T. 1999. Viscous shock-layer simulation of airflow past ablating blunt body with carbon surface. *J. Thermophys. Heat Transf.* 13(1):50–59